JOURNAL OF SPACECRAFT AND ROCKETS
Vol. 32, No. 2, March–April 1995

Scattered Electromagnetic Field of a Re-Entry Vehicle

J. S. Shang* and Datta Gaitonde†
U. S. Air Force Wright Laboratory, Wright-Patterson Air Force Base, Ohio 45433-7913

Scattered electromagnetic fields around the X24C lifting body illuminated by both transverse electric and transverse magnetic incident plane waves are simulated. The refractive and diffractive phenomena are studied in the resonant and the optical regimes. The numerical solutions are generated by solving the three-dimensional Maxwell equations in the time domain using an upwind-biased finite-volume algorithm. The numerical results are third order accurate in space and second order accurate in time. The simulations are validated on simpler shapes, including a cylinder and a sphere, for which the solutions are well known. The scattered field is then described for the re-entry vehicle in the resonant and optical regimes. The numerical results demonstrate that accurate radar cross sections can be obtained by implementation of consistent boundary conditions developed for a perfectly conducting scatterer.

Nomenclature

$\mathbf{B}$	= magnetic flux density, Wb/m^2
$\mathbf{D}$	= electric displacement, C/m^2
$\mathbf{E}$	= electric field intensity, V/m^2
f	= wave frequency, s^{-1}
$\mathbf{H}$	= magnetic flux intensity, A/m
i, j, k	= index of discretized volume
$\mathbf{J}$	= electric current density, A/m^2
$\hat{\mathbf{n}}$	= outer normal of a surface
R	= numerical residual
r, θ, ϕ	= spherical coordinates
t	= time, s
U	= dependent variables
V	= elementary cell volume, m^3
ϵ	= electric permittivity, F/m
λ	= wavelength, m
μ	= magnetic permeability, H/m
ξ, η, ζ	= general curvilinear coordinates
ω	= angular frequency of wave, s^{-1}

Subscripts

ch	= characteristic time required for wave to traverse one body length
i	= incident field property

Superscripts

$+, -$	= flux vector associated with positive and negative eigenvalue

Introduction

REDUCED detectability of advanced fighter aircraft has been identified as one of the four critical areas of aeronautical technology for 2000.[1] The fundamental physical process of infrared or radar signature is based on the refraction and diffraction of electromagnetic waves on a scatterer. The quantity of primary interest is the distribution of electromagnetic energy at a large distance from the scatterer.[2–4] In engineering applications, two techniques commonly adopted for radar signature evaluation are the method of moments and the geometrical theory of diffraction. The former is an accurate boundary-value analysis of the electromagnetic-wave interaction for incident waves at a fixed frequency.[5] The latter has provided an asymptotic analysis in the high-frequency regime.[6] Computational electromagnetics has emerged to meet the technical need to examine the complete range of scattering phenomena at varying frequencies, from the low-frequency Rayleigh through the resonant and optical regimes.[7,8] The basic scientific issue in developing a numerical simulation capability for radar cross section (RCS) is focused on solving the time-dependent, three-dimensional Maxwell equations.

The procedure for deducing the RCS of a scatterer is well known[9,10]: it involves sampling by Fourier transformation of a solution of the Maxwell equations from time to frequency domain, then using field equivalences to transform the near-field scattering results to the far field. For investigation of wave-refracting and -diffracting phenomena in three-dimensional space and time, a large number of discretizing points must be processed. Numerical accuracy and efficiency for RCS analysis still require substantial improvement to make computational electromagnetics a viable simulation tool.

The Maxwell equations in the time domain constitute a hyperbolic partial differential equation system. All known numerical schemes suitable for solving time-dependent initial-value problems will contain dispersive and dissipative errors. These quasiphysical errors can be controlled by a judiciously selected mesh-point system. However, in addition to the approximation inherent in the adopted algorithm, errors are also incurred by the specification of values on the physical or numerical boundaries. This follows from the need to discretize the initial-value problem onto a computer with a finite memory size.[8] The numerical boundary has been known to induce wave reflection, which in turn produces distortion of wave propagation and its energy content. Several absorbing boundary conditions have been developed to overcome this inherent shortcoming.[11,12] However, only the application of characteristic formulation to the Maxwell equations can in principle completely eliminate the fundamental dilemma.[13–15]

On the interface between two dielectric media, such as a scatterer surface, the impinging wave will in general be partially transmitted and partially reflected. Rigorous boundary conditions on the interface can be derived from the integral form of the Maxwell equations.[3,16] In essence, these boundary conditions require the tangential components of electric field intensity and the normal component of magnetic field intensity to be continuous across the interface. Unfortunately, some of these conditions require the knowledge of the surface current density and the surface charge density, which are not known a priori.

The shortage of information at an interface has been circumvented in computational electromagnetics with creative approaches. One effective approach employs staggered grid systems for the electric and magnetic fields.[7,9] Across the interface, derivatives of the electric field on one grid system provide the necessary data to generate the temporal advance of the magnetic field and to sustain the computations. On a unified mesh system for both electric and magnetic

Received Jan. 25, 1994; revision received June 8, 1994; accepted for publication June 19, 1994. This paper is declared a work of the U.S. Government and is not subject to copyright protection in the United States.

*Senior Scientist. Fellow AIAA.
†UES, Inc.; Visiting Scientist, CFD Research Branch, Aeromechanics Division. Member AIAA.

fields, the perfect-shift condition of a numerical solution and the one-dimensional characteristics have also been used effectively in computational electromagnetics.[17,18] In spite of the fact that illustrative achievements have been attained, few assessments have been made in analyzing the accuracy of commonly adopted numerical boundary conditions. In numerical simulations, only different boundary conditions generate different physics from an identical governing equation system.[19] The fidelity to physics is also determined by the accuracy of initial and boundary values as well as the manner in which they are implemented. It may be obvious that developing a rigorous and systematic procedure for numerical boundary conditions across an interface of two media should be a pacing item in computational electromagnetics research.

In the present effort, the scattered field of a complete aerospace vehicle, the X24C-10D, is generated by an upwind-biased finite-volume procedure that is third order accurate in space and second order accurate in time.[15] The interaction of electromagnetic waves with this perfectly conducting scatterer is studied for both transverse electric and magnetic incident waves traveling in the direction of the positive x coordinate. The selection of this configuration is principally dictated by the fact that a single-block body-conformal grid system is readily available.[20–22] Validation of the present results is achieved with a systematic procedure. First, the numerical boundary conditions on a scatterer are compared with an asymptotic formulation in the optical limit.[3] Then, the method is applied to a perfectly conducting cylinder and sphere in the lower optical regime. The resultant radar signature of the cylinder is compared with known results to verify the complete process for radar cross-section analysis.[9] Finally, the scattered fields of the X24C are simulated; the specific comparison with measurement will be documented in future effort.

Analysis

Formulation

The three-dimensional Maxwell equations and constitutive relations in the time domain are[16,23]

$$\frac{\partial(\mu\mathbf{H})}{\partial t} + \nabla \times \mathbf{E} = 0 \tag{1}$$

$$\frac{\partial(\epsilon\mathbf{E})}{\partial t} + \nabla \times \mathbf{H} = -J \tag{2}$$

$$\nabla \cdot \mathbf{B} = 0, \qquad \mathbf{B} = \mu\mathbf{H} \tag{3}$$

$$\nabla \cdot \mathbf{D} = 0, \qquad \mathbf{D} = \epsilon\mathbf{E} \tag{4}$$

The only conservation law, for electric charge and current density, is

$$\frac{\partial \rho}{\partial t} + \nabla \cdot \mathbf{J} = 0 \tag{5}$$

The system of governing equations cast in vector form on a general curvilinear and body conformal coordinate system acquires the following form:

$$\begin{aligned} \xi &= \xi(x, y, z) \\ \eta &= \eta(x, y, z) \\ \zeta &= \zeta(x, y, z) \end{aligned} \tag{6}$$

$$\frac{\partial \hat{U}}{\partial t} + \frac{\partial \hat{F}}{\partial \xi} + \frac{\partial \hat{G}}{\partial \eta} + \frac{\partial \hat{H}}{\partial \zeta} = -\hat{J} \tag{7}$$

The transformed dependent variables and the flux vectors, $\hat{F}$, $\hat{G}$, and $\hat{H}$ in the above equations are given in the following;

$$\begin{aligned} &\hat{U} = UV, \qquad \hat{J} = JV, \qquad \hat{F} = (\xi_x F + \xi_y G + \xi_z H)V \\ &\hat{G} = (\eta_x F + \eta_y G + \eta_z H)V, \qquad \hat{H} = (\zeta_x F + \zeta_y G + \zeta_z H)V \end{aligned} \tag{8}$$

where

$$U = \begin{Bmatrix} B_x \\ B_y \\ B_z \\ D_x \\ D_y \\ D_z \end{Bmatrix}, \qquad F = \begin{Bmatrix} 0 \\ -D_z/\epsilon \\ D_y/\epsilon \\ 0 \\ B_z/\mu \\ -B_y/\mu \end{Bmatrix} \tag{9}$$

$$G = \begin{Bmatrix} D_z/\epsilon \\ 0 \\ -D_x/\epsilon \\ -B_z/\mu \\ 0 \\ B_x/\mu \end{Bmatrix}, \quad H = \begin{Bmatrix} -D_y/\epsilon \\ D_x/\epsilon \\ 0 \\ +B_y/\mu \\ -B_x/\mu \\ 0 \end{Bmatrix}, \quad J = \begin{Bmatrix} 0 \\ 0 \\ 0 \\ J_x \\ J_y \\ J_z \end{Bmatrix} \tag{10}$$

A cell-centered, finite-volume scheme based on the MUSCL approach is adopted for the present study.[15] The finite-volume scheme discretizes the differential formulation into a difference presentation astride the elementary cell surface:

$$\frac{\Delta \hat{U}}{\Delta t} + \frac{\Delta \hat{F}}{\Delta \xi} + \frac{\Delta \hat{G}}{\Delta \eta} + \frac{\Delta \hat{H}}{\Delta \zeta} - \hat{J} = \frac{\Delta \hat{U}}{\Delta t} + R = 0 \tag{11}$$

where the continuous operators $\partial/\partial t$, $\partial/\partial \xi$, $\partial/\partial \eta$, $\partial/\partial \zeta$ have been replaced by the discrete operators $\Delta/\Delta t$, $\Delta/\Delta \xi$, $\Delta/\Delta \eta$, $\Delta/\Delta \zeta$, and where R denotes the residual of the numerical approximation. The discrete operators Δ describe the flux balance on all cell faces including the boundaries of the scatterers.

The construction of the flux vectors F, G, and H at the interface of each cell adopts the concept of splitting introduced by Steger and Warming for CFD.[24] The flux at any cell surface is formed by a superposition of two components, F^+, G^+, H^+ and F^-, G^-, H^-, according to the signs of their eigenvalues. Physically, this unique relationship honors the direction of signal propagation. Since the diagonalization of the Maxwell equations can only be achieved in a single spatial direction at a time, the flux splitting is performed in the one-dimensional time-space plane. Under this circumstance, the positive and the negative components represent the right and the left running waves within the domain of influence[13,14,24,25]:

$$\begin{aligned} F_{i+\frac{1}{2}} &= F^+\left(U^L_{i+\frac{1}{2}}\right) + F^-\left(U^R_{i+\frac{1}{2}}\right) \\ G_{j+\frac{1}{2}} &= G^+\left(U^L_{j+\frac{1}{2}}\right) + G^-\left(U^R_{j+\frac{1}{2}}\right) \\ H_{k+\frac{1}{2}} &= H^+\left(U^L_{k+\frac{1}{2}}\right) + H^-\left(U^R_{k+\frac{1}{2}}\right) \end{aligned} \tag{12}$$

In the above, the superscripts L and R refer to the reconstructed solution on either side of an interface.

The numerical accuracy of this finite volume scheme is actually determined by the construction of the states, U^L and U^R, from the known values of the solution in the adjacent cells. The present method adopts the upwind-biased algorithm due to van Leer.[26,27] The two states at any interface are constructed by a windward-biased formula:

$$U^L_{i+\frac{1}{2}} = U_i + \frac{\phi}{4}[(1-\kappa)\nabla + (1+\kappa)\Delta]U_i \tag{13}$$

$$U^R_{i+\frac{1}{2}} = U_{i+1} - \frac{\phi}{4}[(1+\kappa)\nabla + (1-\kappa)\Delta]U_{i+1} \tag{14}$$

where $\nabla U_i = U_i - U_{i-1}$ and $\Delta U_i = U_{i+1} - U_i$. The basic algorithm is third-order accurate in space when $\kappa = \frac{1}{3}$. In this case, since the leading truncation error term is the fourth-order derivative, dissipative errors may be expected to dominate.

For finite-volume schemes, the balancing of split fluxes on the interface of cells is achieved in an orthogonal coordinate system one

axis of which is locally aligned with the cell surface outward normal. Therefore, the needed locally orthogonal coordinates depend only on the shape and edges of the cell in consideration. Since the tangential vectors of a point on any surface are nonunique, two internally consistent tangential components are constructed by consecutive cross products.[15] The resultant locally orthogonal coordinate system reduces to the Cartesian frame, in which the necessary information on eigenvalues and eigenvectors for flux splitting is known.[13,15] In addition, the direction cosines are symmetrical with respect to the two coordinate systems; thus the inverse transformation from the (ξ, η, ζ) space to the locally orthogonal system is simply given by the transpose of the metric of coordinate transformation. The calculation details of split fluxes can be found in our earlier effort.[15]

The time integration method employs the Runge-Kutta family of single-step, multistage procedures.[28] Although this basic scheme is capable of higher-order resolution in time, only the two-stage, formally second-order accurate algorithm called Heun's scheme is used, as described in Ref. 15. Therefore, the present solution is an accurate numerical approximation to third order in space and second order in time.

Boundary Conditions

For time-dependent scattering-field calculations, the computational boundaries consist of the far-field limits and the scatterer surface. The former are a consequence of performing the simulation on computers with limited memory space; the latter is a physical requirement for wave motion across media of different dielectric properties.

The far-field boundary arises from the necessity of imposing numerical boundary conditions on an initial-value problem in a truncated space.[8,13,17] Through this threshold, disturbances will propagate to and from the interior of the computational domain. These discretized errors invariably induce spurious reflected waves from the computational boundary. The problem is most critical for numerical simulations concerned mainly with diffracting and refracting phenomena, where the poor numerical accuracy of the nonphysical reflecting waves will result in erroneous accumulations of radiation energy.[8]

The undesirable reflection from numerical boundaries can be eliminated by the characteristic formulation.[13–15] The fundamental idea of this approach for solving a hyperbolic system of equations is derived from eigenvalue and eigenvector analysis.[13,25] From the field-action approach, differential geometry yields a domain of influence partitioned by characteristics.[29] At present the characteristic formulation has an inherent limitation in that the coefficient matrices of the governing equations can be diagonalized only in one dimension at a time. Nevertheless, in computational electromagnetics this limitation does not become overly restrictive, because the direction of wave travel is always known to be that of $\mathbf{E} \times \mathbf{H}$. The coordinates at far field can be made to align with the principal axis of wave motion. Along the one-dimensional time-space trajectories, information will propagate as invariants. Therefore, the far-field condition on the truncated boundary is approximated simply by the zero incoming flux component,[13,15]

$$F^{-}(\xi, \eta, \zeta) = 0 \tag{15}$$

This condition is implemented on the wave exit plane to allow the incident and reflected waves to propagate away from the computational domain.

The physical requirement on the surface of a scatterer with a finite Gaussian curvature is that the total tangential electric field and the normal magnetic field be continuous across the boundary.[2,16] On a stationary surface, the Maxwell equations in integral form yield the following boundary conditions[16,23]:

$$\begin{aligned} \hat{\mathbf{n}} \times (\mathbf{E}_1 - \mathbf{E}_2) &= \mathbf{0} \\ \hat{\mathbf{n}} \times (\mathbf{H}_1 - \mathbf{H}_2) &= \mathbf{J}_s \\ \hat{\mathbf{n}} \cdot (\mathbf{B}_1 - \mathbf{B}_2) &= 0 \\ \hat{\mathbf{n}} \cdot (\mathbf{D}_1 - \mathbf{D}_2) &= \rho_s \end{aligned} \tag{16}$$

On a perfect conductor surface, the tangential components of total electric field are required to vanish. This requirement implies that the normal component of the total magnetic field is zero on the scatterer surface.[2,16,23] Although the volume current and charge densities may be infinite on a perfect conductor, the surface current and charge densities can still be defined by a limiting process.[16] For the present analysis, the unknown surface current and charge densities are treated as finite jumps of constant value. This assumption allows three additional derivatives to be introduced as boundary conditions:

$$\begin{aligned} \hat{\mathbf{n}} \cdot \nabla[\hat{\mathbf{n}} \times (\mathbf{H}_1 - \mathbf{H}_2)] &= 0 \\ \hat{\mathbf{n}} \cdot \nabla[\hat{\mathbf{n}} \cdot (\mathbf{D}_1 - \mathbf{D}_2)] &= 0 \end{aligned} \tag{17}$$

The system of boundary conditions is therefore closed and can be solved by two 3×3 matrices. Validation of the imposed boundary approximations can be accomplished by comparing with solutions generated by analytic boundary values. The theoretical result for an plane wave impinging on an infinite planar surface has been derived from the standard Fresnel formula.[2,3] In the optical limit, the analytic total field values on the conducting surface have been obtained from the law of reflection by Kay[3] and are recorded here for later validation:

$$\mathbf{E} = 2[\mathbf{E}_i - \hat{\mathbf{n}} \times (\mathbf{E}_i \times \hat{\mathbf{n}})] \tag{18}$$

and

$$\mathbf{H} = 2[\mathbf{H}_i - (\hat{\mathbf{n}} \cdot \mathbf{H}_i)\hat{\mathbf{n}}] \tag{19}$$

where $\mathbf{E}_i$ and $\mathbf{H}_i$ correspond to the incident plane wave traveling along the x coordinate. Both the transverse electric (TE) and transverse magnetic (TM) waves are described by a sinusoidal wave in time and space. The angular frequency Ω of the incident wave is given as[23]

$$\Omega = 2\pi f \tag{20}$$

and the wavelength λ is defined by the distance over which the phase of the wave increases by 2π:

$$\lambda = \frac{1}{\sqrt{\mu\epsilon} f} = \frac{2\pi}{\sqrt{\mu\epsilon}\Omega} \tag{21}$$

Since the speed of light, $\sqrt{\mu\epsilon}$, is scaled out of the present formulation, the ratio of the characteristic scatterer dimension L to the wavelength of the incident wave is given by

$$\frac{L}{\lambda} = \frac{\Omega L}{2\pi} \tag{22}$$

For all the numerical simulations, this ratio is taken within the range from 1 to 10, which spans the scattering regimes from resonance to the lower optical limit.[2–4]

Numerical Procedure

The numerical procedure used in the present analysis is the spatially third-order- and temporally second-order-accurate upwind-biased, cell-centered finite-volume scheme.[15] Although characteristic-based algorithms have been mapped onto distributed-memory computers such as the Intel Touchstone Delta and the Paragon multicomputers, these efforts are still in the developmental stage.[30,31] The numerical efficiency of these computer codes is impressive, particularly the finite-difference code,[13] which has attained a scalable data procession rate of more than 6.5 gigaops on a data structure of $512 \times 96 \times 96$. However, additional improvement is still required for practical applications. In the present effort only the version of the code for a shared-memory system is used. On the Cray C90, the present computer code achieves a rate of 572 megaflops on a single processor, corresponding to a data-processing rate of 3.398×10^{-6} seconds per node per time step.

The present algorithm is validated by prediction of the scattering from simple shapes for which the solutions are well known. These simple configurations include the cylinder and the sphere. In every calculation, each wavelength is supported by at least 18 nodes. The mesh systems cover a range of dimensions and are described with the results.

All computations were initiated from a quiescent computational domain excited by incident TE or the TM planar waves. The temporal advancement was sustained for a period of time that allowed the incident wave and its reflection to traverse the entire computational domain at the unperturbed phase velocity ($t = 2t_{ch}$, where t_{ch} is the time required for a wave to traverse the length of the domain). The radar signature was calculated for scattering by a cylinder. For this, the temporal data are further processed by an FFT procedure for a selected sampling period, followed by the application of the near-field-to-far-field transformation according to the equivalence principle.[2–4,9,10]

Discussion of Results

The implementation of the boundary conditions is first assessed by comparing the results immediately adjacent to the surface of a perfectly conducting sphere with theory. Next, the overall procedure is examined by comparison of the radar cross section of a cylinder with a known solution.[9] The scattered three-dimensional field of a sphere is also simulated. Finally, calculations on scattering due to the X24C are described for two distinct excitations, both with TE and TM incident plane waves and over a range of wavelengths. In order to eliminate the errors incurred by Fourier sampling and the application of the near-field-to-far-field transformation, only the scattered fields are presented.[7–9] The detailed comparison with signature analysis is deferred to the near future.

Figure 1 presents the absolute value of the computed x component of the total electric field on the cell immediately adjacent to the surface of a conducting sphere. The electromagnetic field is excited by an incident TE wave propagating along the negative direction of the z axis with a diameter-to-wavelength ratio of one. The numerical result was recorded at the instant when the incident TE wave had traversed the beam path 5.823 times ($t = 5.823t_{ch}$). These data in the equatorial plane of the conducting sphere are presented together with the theoretical value over the entire look angle[3]. In spite of the fact that the solution was generated on a fairly coarse mesh system ($25 \times 24 \times 48$), the only noticeable departure from the theoretical value is contained in the overlapping area between shadow and exposed regions. It is also noteworthy that the present numerical result is simulated in the resonant scattering regime, and the theoretical value is an asymptote in the optical limit.

Results on a refined ($49 \times 48 \times 96$) mesh system are in excellent agreement with theory, as shown in Fig. 2. Within the limits of truncation error, results from these two entirely different approaches are indistinguishable. The excellent agreement between the analytic and numerical boundary even extends to include the overlapping area between the exposed and the shadow regions. This demonstrates that the present boundary condition for a perfectly conducting scatterer is accurate and is able to replicate the physical law for refraction. More importantly, the results indicate that these conditions are valid for high-frequency refracting and diffracting phenomena up to the optical scattering regime.

Additional substantiation can be deduced from a direct comparison at a distance of 1.615 radii from the sphere, Fig. 3. At this location, the numerical discrepancy appears as a consequence of quasiphysical error inherited from the numerical algorithm. Since the incident wave is described on the sphere surface for the analytic boundary-value approach, the reflected wave only propagates outward in a single path. On the other hand, using the present approximate boundary condition, one has to compute the reflection of the incident wave that propagates from the far-field boundary to the body surface. The disparity between the solutions is similar to what one would anticipate from the differences between the total- and scattered-field formulations. The maximum difference between solutions is less than 4% and mostly originates from the overlapping area of the exposed and shadow regions. In this region, the analytic result based on the specular reflection law has reached its limit of validity.[2–4]

A final evaluation of the accuracy of the boundary condition can be assessed with the scattering of a TM wave by a cylinder. For this calculation, the diameter of the cylinder is assumed to be unity, while the incident wavelength is π. The outer boundary is located at two wavelengths from the body, the region being discretized by a 60×60 mesh. Thus, the wave is resolved with 30 and 60 points in the radial and circumferential directions respectively. The accuracy of the boundary conditions may be assessed by examining the quantity $\nabla \cdot \mathbf{H}$, which should be identically zero. Figure 4 exhibits the unnormalized computed value of $\nabla \cdot \mathbf{H}$ for the planar incident field imposed on the cylindrical polar coordinate system. The nonzero values provide an estimate of the error in the evaluation process for $\nabla \cdot \mathbf{H}$, consisting not only in the truncation error of the formula but also in the lack of mesh alignment with the incident wave in some regions. This figure thus provides an error bound on the present numerical procedure. Figure 5 shows $\nabla \cdot \mathbf{H}$ at $t = 15t_{ch}$, i.e., after the incident wave has traversed the length of the domain 15 times. A direct comparison of Figs. 4 and 5 reveals a strong resemblance of the error pattern. These observations confirm that the present

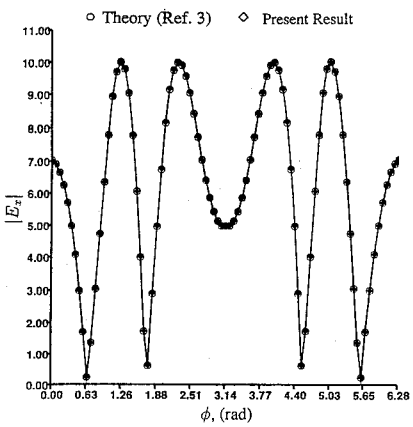

Fig. 2 Absolute value of total electric field adjacent to surface of a conducting sphere—$49 \times 48 \times 96$ mesh: $R = R_b$ and $T = 5.8T_{ch}$.

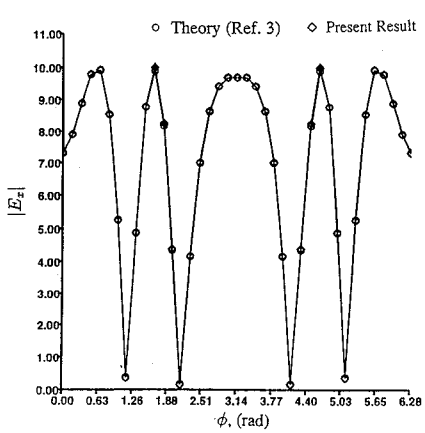

Fig. 1 Absolute value of total electric field adjacent to surface of a conducting sphere—$25 \times 24 \times 48$ mesh: $R = R_b$ and $T = 5.8T_{ch}$.

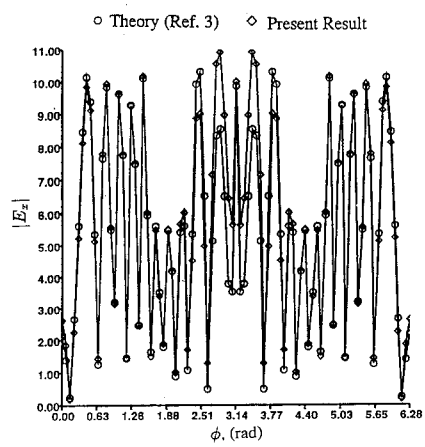

Fig. 3 Conducting sphere field at 1.615 radii from sphere—$49 \times 48 \times 96$ mesh: $R = R_b$ and $T = 5.8T_{ch}$.

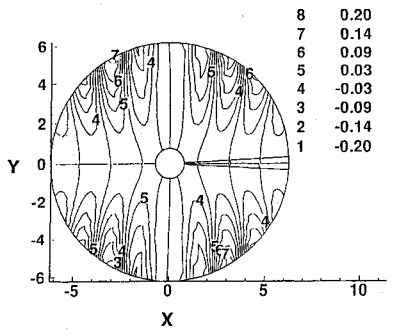

Fig. 4 Divergence of incident magnetic field for cylinder $T = 0.0$, grid system (60,60).

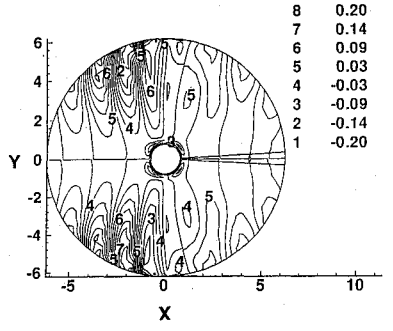

Fig. 5 Divergence of total magnetic field for cylinder—$T = 15T_{ch}$, grid system (60,60).

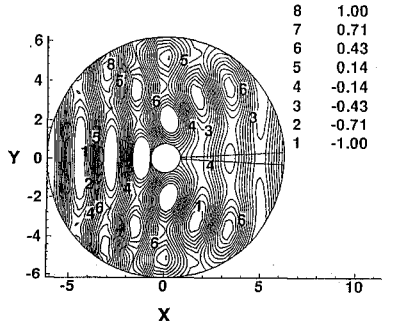

Fig. 6 Total electric field for cylinder—$T = 15T_{ch}$, grid system (60,60).

boundary condition satisfies the governing equation equally well in the computational region immediately adjacent to the body, and establishes itself as a viable approximation.

The contour presentation of the total electric field is given in Fig. 6. The numerical result reveals a wave pattern consistent with that commonly observed in the pioneering efforts.[2,8,9,17,18] Unfortunately, for a time-dependent problem, the volume of the data is massive, which makes display difficult, and the transformation of temporal data from time to frequency domain is contingent on the sampling process. Precise comparison of numerical results in the time domain is critical but difficult to achieve. Additional and improved verification procedures for computational electromagnetics in the time domain must be developed in the future.

The radar cross section of the above perfectly conducting cylinder is presented in Fig. 7. The four numerical results obtained with different time increments (CFL = 0.5 and 1.0), instants ($t = 15t_{ch}$ and $20t_{ch}$), and periods of sampling ($\lambda = 1.0$ and 2.0) are essentially identical. The normalized radar cross section by wavelength exhibits excellent agreement to that of Umashankar and Taflove.[9] The agreement between the two numerical results in the region exposed to the impinging wave is limited only by the digitized data accuracy from the graph of the archive.[9] The maximum difference between the two results is located within the shadow region with respect to the incident wave and is less than about 3%.

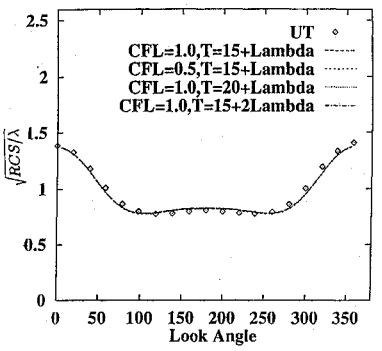

Fig. 7 Radar cross section of cylinder—grid system (60,60).

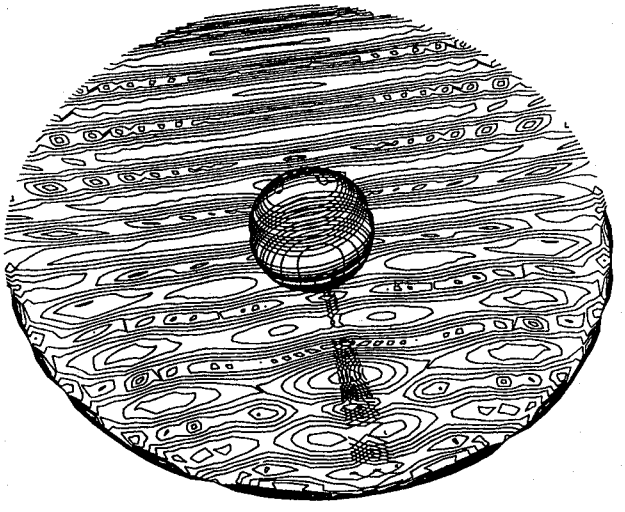

Fig. 8 Scattered electric field around conducting sphere—incident TE plane wave—49 × 48 × 96 mesh: $R = R_b$ and $T = 5.8T_{ch}$.

However, it is uncertain what portion of the discrepancy was introduced by the FFT time sampling and by the near-field-to-far-field transformation. Nevertheless, the present result has demonstrated our ability to predict an accurate signature of electromagnetic waves.

Figure 8 depicts a perspective view of the magnitude of the scattered electric field around a conducting sphere excited by a TE planar incident wave that travels along the negative z axis and has a wavelength-to-diameter ratio of one. Therefore the simulated interacting-wave phenomenon belongs to the resonant scattering regime. The entire computational domain is described by two concentric spheres; the outer sphere has a diameter 1.5 times the inner sphere. The numerical results are generated on a $49 \times 48 \times 96$ mesh system and displayed at an instant $t = 5.6t_{ch}$. The intensely interacting wave pattern in the region exposed to the incident wave is clearly evident on the meridional plane of the spherical space. In sharp contrast to that exposed region, the scattered wave pattern is rather unperturbed in the shadow region and beyond. In all, the projection of wave structure strongly resembles that of the earlier cylindrical simulation, Fig. 6. However, additional wave structures are also detectable in the region linking the exposed and the shadow regions. Since a validation by a specific comparison with another result in the time domain is unavailable at this time, no further attempt is made to interpret the present result and its connection with the possible resolution of the creeping and surface waves around this specific scatterer.[2–4]

As independent verification for the scattering simulation of the sphere, the y component of the scattered electric intensity (E_y) and the z component of the scattered magnetic intensity (H_z) are shown in Fig. 9. Along the z ordinate and in the domain exposed to the incoming TE wave, the amplitude of the reflected wave is double the incident value. For a perfectly conducting sphere, the electromagnetic energy of the incident wave cannot be transmitted

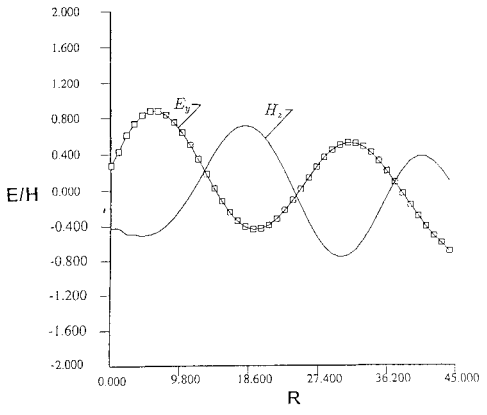

Fig. 9 Scattered electric and magnetic field for sphere along backscattered ray—49 × 48 × 96 mesh: $T = 5.8$.

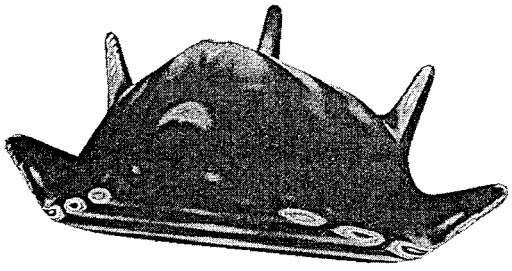

Fig. 10 Scattered electromagnetic-wave magnitude adjacent to scaled X24-10D model—TE excitation, 91 × 29 × 160 mesh.

to the scatterer.[2,4,23] As the consequence, the amplitudes of E_y and H_z of the reflected wave are twice those of the incident wave. The present numerical results exhibit the correct physical behavior at a point where the surface outward normal coincides with the incoming ray, and the numerical error is only 2% of the amplitude of the wave. In the shadow region opposite to the incident wave (not shown), the scattered fields E_y and H_z nearly vanish near the scatterer, and reveal mild distortion as the wave exits the computational domain.

The X24C-10D re-entry vehicle was designed as an air-launched, rocket-powered, high-lift-to-drag-ratio vehicle for Mach 6 and higher. The geometry is complex, and is chosen for study because it contains several features typical of hypersonic aircraft. In addition to a blunt-leading-edge spherical nose and a relatively flat delta-shaped underbody, the aft portion consists of a system of five fins—a central fin, two middle fins, and two strakes. The mesh employed consists of a single block enveloping the configuration. Upstream of the vehicle, the line $\xi = 0$ corresponds to a spherical polar singularity. Since the surface area of each cell face on this plane is identically zero, the total flux $\hat{F}$ is zero and is so specified. Downstream and on the surface, the no-reflection and perfectly-conducting-surface conditions are imposed as described previously. The incident field is prescribed at two points on and adjacent to the outer ($\eta = 1$) surface. All of the simulations assume a plane wave (TM or TE) traveling in the x direction, i.e., at zero angle of attack. In the circumferential or spanwise direction, two-point overlap is employed both for $\zeta = 0$ and $\zeta = 1$ mesh surfaces. This periodic condition assures proper information propagation and analytic continuity across these faces.

Several calculations on the scaled model of this vehicle are now described. The cases examined span a range of ratios of characteristic length (body length) to wavelength, reproducing phenomena from the resonant to the lower limit of the optical regimes. The TM and TE excitations are imposed separately. For the purposes of brevity, the details of only a few of the calculations are presented.

The magnitudes of scattered electromagnetic waves immediately adjacent to the surface due to TE excitation are presented in Figs. 10 and 11 for characteristic-length-to-wavelength ratios L/λ of 2.3 and 9.2, respectively. For the former, the supporting grid system consists of 91 × 29 × 160 volumes; for the latter, 181 × 59 × 162 volumes.

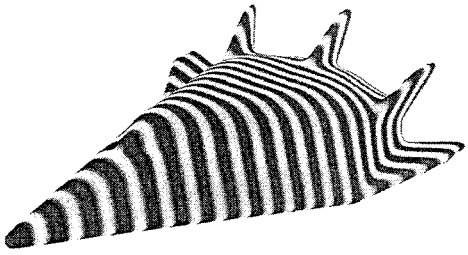

Fig. 11 Scattered electromagnetic-wave magnitude adjacent to scaled X24-10D model—TE excitation, 181 × 59 × 162 mesh.

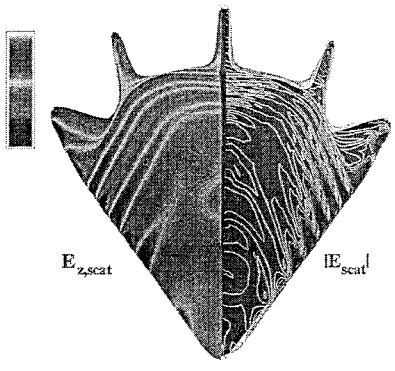

Fig. 12 Scattered electromagnetic-wave magnitude adjacent to scaled X24-10D model—TM excitation, 65 × 28 × 110 mesh.

The first coordinate index indicates the number of streamwise stations defining the computational domain, which includes the entire configuration. The second index describes the number of cells between the body surface and the far field, and the third index gives the number of cells used to circumscribe the cross-sectional planes of the re-entry vehicle. In each of these cases, a single wavelength in any direction is resolved by no less than 18 cells. The peaks and valleys of the scattered wave amplitude projected on the vehicle surface display a structured fringe. The principal difference between the two simulations lies in the density of the fringe pattern: the higher the incident wave frequency, the greater the number of the fringes. Another salient feature of the scattered fields is expressed by the surface curvature: the smaller the radius of surface curvature, the broader the diffraction pattern. All numerical results exhibit highly concentrated contours at the chine of the forebody and the leading edge of strakes and fins.

Calculations with TM excitation also span a range of characteristic-length-to-wavelength ratios, from 2.3 to 9.2. For the smaller ratios, the mesh system employed is somewhat coarser but nevertheless sufficient to support each wavelength by at least 15 nodes. Figure 12 exhibits contours of scattered E_z on the left portion of the vehicle and the magnitude of the scattered electric field on the right for $L/\lambda = 4.6$ on a 65 × 28 × 110 mesh. It is evident that in the contour presentation, there are no significant qualitative distinguishing features between this TM pattern and the TE wave excitation presented earlier, although the details and the processed signature are undoubtedly different.[2–4] The dominant variation in the scattered field, its magnitude as well as its z component, is once again observed in the low-radius-of-curvature chine region (formed by the intersection of the relatively flat lower surfaces and sides of the vehicle).

Figure 13 displays the z component of the electric field: on the left the scattered field, and on the right the total field at the first mesh point away from the surface. The total-field variation also shows the same high intensity variation in regions of curvature. For this simulation, the features induced by the canopy region are also highlighted by this effect. The pronounced fringe pattern is partly due to the increased frequency of the incident wave and partly to improved resolution. The total E_z value is seen to decrease to zero near the symmetry plane. This is anticipated, because the top portion of the aircraft becomes nearly tangential to a z = constant plane and the imposed boundary condition for the perfect conductor enforces

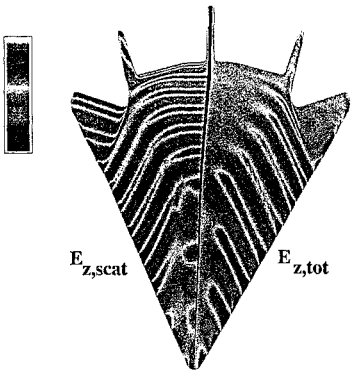

Fig. 13 Scattered electromagnetic-wave magnitude adjacent to scaled X24-10D model—TM excitation, 90 × 55 × 162 mesh.

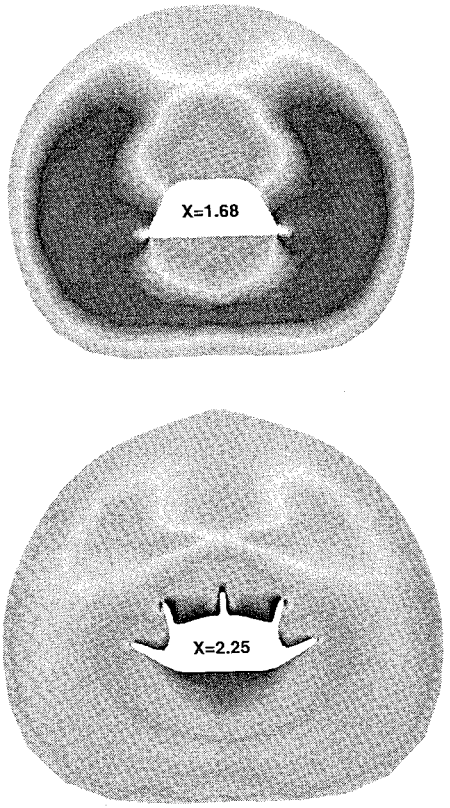

Fig. 14 Electromagnetic field at selected cross-section planes, TE excitation.

this result. A similar situation also holds for the lower and relatively flat portion of the aircraft.

The reflections and diffractions of the wave around the X24C-10D on selected cross-sectional planes are given in Fig. 14. These sections span the region of the aircraft downstream of the canopy to the trailing portion of the re-entry vehicle. In general, the reflection and diffraction patterns are similar to the shock-wave structure encountered in computational aerodynamic simulation. The similarity is particularly pronounced in regions bounded by the strake, middle fin, and central fin, where multiple wave reflection is observed. The broadening of diffraction pattern on surfaces on which the radius of curvature is significantly smaller is also easily identifiable. In this respect, computational electromagnetics not only requires the processing of a large number of data for high-frequency wave motion, but also needs better resolution in body definition than computational fluid dynamics.

Concluding Remarks

The cell-centered, upwind-biased finite-volume procedure developed in previous work is demonstrated to be equally effective in simulating the reflecting and diffracting phenomena induced by a simple scatterer as well as a complex aerospace vehicle. Excellent agreement is achieved for simpler two- and three-dimensional objects for which validating data are available in the form of radar cross sections and asymptotic theory.

The characteristic formulation shows potential to significantly reduce the spurious wave reflection from the numerical boundary at the far field. More importantly, the consistent boundary conditions developed by the present analysis for the perfectly conducting scatterer have demonstrated their validity in both the resonant and the optical scattering regimes. Additional and continuous validation of the present numerical procedure is still required by developing and seeking support from physical measurements in the time domain.

Acknowledgment

The authors gratefully acknowledge the support in grid-system generation by John S. Seo of the Aeromechanics Division, Flight Dynamics Directorate, Wright Laboratory.

References

[1]Korkegi, R. H. (ed.), "Aeronautical Technology 2000: A Projection of Advanced Vehicle Concepts, National Research Council Report," National Academy Press, Washington, 1985.

[2]Brown, J. J., Senior, T. B. A., and Uslenghi, P. L. E. (eds.), *Electromagnetic and Acoustic Scattering by Simple Shapes*, Hemisphere, New York, 1987, pp. 353–413.

[3]Crispin, J. W., and Siegel, K. M. (eds.), *Methods of Radar Cross-Section Analysis*, Academic, New York, 1968, pp. 3–32.

[4]Knott, E. F., Shaeffer, J. F., and Tuley, M. T., *Radar Cross Sections*, Artech House, Boston, 1993, pp. 156–188.

[5]Harrington, R. F., *Field Computation by Moment Methods*, Macmillan, New York, 1968.

[6]Keller, J. B., "Geometrical Theory of Diffraction," *Journal of the Optical Society of America*, Vol. 52, 1962, p. 116.

[7]Yee, K. S., "Numerical Solution of Initial Boundary Value Problems Involving Maxwell's Equations in Isotropic Media," *IEEE Transactions on Antennas and Propagation*, Vol. 14, 1966, pp. 302–307.

[8]Taflove, A., "Re-Inventing Electromagnetics: Supercomputing Solution of Maxwell's Equations via Direct Time Integration on Space Grids," *Computing Systems in Engineering*, Vol. 3, No. 1-4, 1992, pp. 153–168.

[9]Umashankar, K., and Taflove, A., "A Novel Method to Analyze Electromagnetic Scattering of Complex Objects," *IEEE Transactions on Electromagnetic Compatibility*, Vol. EMC-24, No. 4, 1982, pp. 397–405.

[10]Luebbers, R., Kunz, K. S., Schneider, M., and Hunberger, F., "A Finite-Difference Time-Domain Near Zone to Far Zone Transformation," *IEEE Transactions on Antennas and Propagation*, Vol. 39, No. 4, 1991, pp. 429–433.

[11]Enquist, B., and Majda, A., "Absorbing Boundary Conditions for the Numerical Simulation of Waves," *Mathematics of Computation*, Vol. 31, July 1977, pp. 629–651.

[12]Higdon, R., "Absorbing Boundary Conditions for Difference Approximations to the Multidimensional Wave Equation," *Mathematics of Computation*, Vol. 47, 1986, pp. 437–459.

[13]Shang, J. S., "Characteristic-Based Methods for the Time-Domain Maxwell Equations," AIAA Paper 91-0606, Jan. 1991.

[14]Shang, J. S.,"A Characteristic-Based Algorithm for Solving 3-D, Time Domain Maxwell Equations," AIAA Paper 92-0452, Jan. 1992.

[15]Shang, J. S., and Gaitonde, D., "Characteristic-Based, Time-Dependent Maxwell Equations Solvers on a General Curvilinear Frame," AIAA Paper 93-3178, June, 1993.

[16]Kong, J. A., *Electromagnetic Wave Theory*, Wiley, New York, 1986, pp. 1–27.

[17]Shankar, V., "Research to Application—Supercomputing Trends for the 90's and Opportunities for Interdisciplinary Computations," AIAA Paper 91-0002, Jan. 1991.

[18]Shankar, V., Mohammadian, A. H., and Hall, W. F., "A Time-Domain Finite-Volume Treatment for the Maxwell's Equations," *Electromagnetics*, Vol. 10, 1990, p. 247.

[19]Shang, J. S., "An Assessment of Numerical Solutions of the Compressible Navier–Stokes Equations," *Journal of Aircraft*, Vol. 22, No. 5, 1985, pp. 353–370.

[20]Scherr, S. J., and Shang, J. S., "Three-Dimensional Body-Fitted Grid System for a Complete Aircraft," AIAA Paper 86-0428, Jan. 1986.

[21]Shang, J. S., and Scherr, S. J., "Navier–Stokes Solution for a Complete Re-Entry Configuration," *Journal of Aircraft*, Vol. 23, No. 12, 1986, pp. 881–888.

[22]Gaitonde, D., and Shang, J. S., "Numerical Simulation of Flow Past the X24C Reentry Vehicle," AIAA Paper 93-0319, Jan. 1993.

[23]Harrington, R. R., *Time-Harmonic Electromagnetic Fields*, McGraw–Hill, New York, 1961, pp. 95–132.

[24]Steger, J. L., and Warming, R. F., "Flux Vector Splitting of the Inviscid Gasdynamic Equations with Application to Finite Difference Methods," *Journal of Computational Physics*, Vol. 40, No. 2, 1981, pp. 263–293.

[25]Roe, P. L., "Characteristic-Based Schemes for the Euler Equations," *Annual Review of Fluid Mechanics*, Vol. 18, 1986, pp. 337–365.

[26]van Leer, B., "Flux-Vector Splitting for the Euler Equations," *Inst. for Computer Applications in Science and Engineering*, TR 82-30, Sept. 1982.

[27]Anderson, W. K., Thomas, J. L., and van Leer, B., "Comparison of Finite Volume Flux Vector Splittings for the Euler Equations," AIAA Paper 85-0122, Jan. 1985.

[28]Carnahan, B., Luther, H. A., and Wilkes, J. O., *Applied Numerical Methods*, Wiley, New York, 1969, pp. 361–392.

[29]Sommerfeld, A., *Partial Differential Equations in Physics*, Academic, New York, 1949, pp. 36–42.

[30]Shang, J. S., Hill, K. C., and Calahan, D. A., "Performance of a Characteristic-Based, 3-D Time-Domain Maxwell Equations Solver on a Massively Parallel Computer," AIAA Paper 93-3179, June 1993.

[31]Shang, J. S., Calahan, D., and Vikstrom, B., "Performance of a Finite-Volume CEM Code on Multicomputers," AIAA Paper 94-0236, Jan. 1994.

T. C. Lin
Associate Editor

INTEGRATED PRODUCT AND PROCESS DEVELOPMENT (IPPD) FOR AEROSPACE SYSTEMS

September 22-23 1995
Los Angeles, CA

The aerospace industry needs to do a better job of designing, developing , and manufacturing its products to be competitive.This course will use a generic IPPD methodology to show you how new systems engineering and quality engineering techniques and tools can be integrated into a design trade decision support process using a computer integrated environment.

WHO SHOULD ATTEND
Engineers, managers, and academic faculty involved in the design, development, and manufacturing of aerospace systems will benefit.

HOW YOU WILL BENEFIT FROM THIS COURSE
• Learn how to make better product design trades at the system, subsystem/major component, and sub component/Line Replaceable Unity (LRU)/part levels, as well as enhanced recomposition techniques that include parallel manufacturing and affordability process design trades.

• Learn how emerging information technologies will permit design by function, integrated product-process data and description models, and novel design considerations.

• Discover how a computer integrated environment can build on information technology to allow parallel product and process design trades early in the product development process.

INSTRUCTORS
Led by Dr. Daniel P. Schrage, Georgia Tech Aerospace Systems Deign Laboratory

For more detailed information call or FAX
Johnnie White
Phone: 202/646-7447
FAX: 202/646-7508

AIAA
American Institute of Aeronautics and Astronautics